Defect and Diffusion Forum
ISSN: 1662-9507, Vol. 425, pp 35-42
doi:10.4028/p-6ho92o

Submitted: 2022-09-07
Revised: 2022-11-01
Accepted: 2022-11-25
Online: 2023-05-31

Charge State Control Over Point Defects in SiC Devices

Marianne Etzelmüller Bathen[1,a,*], Gard M. Selnesaunet[2,b], Marius J. Enga[3,c], Snorre B. Kjeldby[1,d], Johanna Müting[2,e], Lasse Vines[2,f], and Ulrike Grossner[1,g]

[1]Advanced Power Semiconductor Laboratory, ETH Zürich, 8092 Zürich, Switzerland

[2]Department of Technology Systems, University of Oslo, 0316 Oslo, Norway

[3]Department of Physics, University of Oslo, 0316 Oslo, Norway

[a]bathen@aps.ee.ethz.ch, [b]g.m.selnesaunet@its.uio.no, [c]mjenga92@gmail.com, [d]s.b.kjeldby@smn.uio.no, [e]johanna.mueting@gmail.com, [f]lasse.vines@fys.uio.no, [g]ulrike.grossner@ethz.ch

Keywords: SiC, Color Centers, Silicon Vacancy, Carbon Antisite-Vacancy Pair, Cathodoluminescence, Density Functional Theory.

Abstract. Point defects in silicon carbide (SiC) are well positioned for integration with SiC based quantum photonic devices due to the maturity of SiC material and fabrication technology, the plethora of candidate quantum emitters that can be formed in SiC, and the potential for emission over a wide spectral range from the visible to the infrared. However, for each of the available color centers in SiC, only one of the charge states has displayed quantum emission, meaning that the emission strongly depends on the Fermi level and hence the doping concentration in the material. In this contribution, we discuss the methodology and mechanism for electrical charge-state control over point defects in SiC devices.

Introduction

Silicon carbide (SiC) is a promising material for power electronics devices, however, recent developments have marked it as equally intriguing for quantum technology applications. Point defects in SiC may trap charge carriers in deep localized states which can allow properties such as single-photon emission and coherent spin manipulation to arise [1]. While the nitrogen-vacancy (NV) center in diamond is arguably still the most famous semiconductor color center for quantum applications [2], interest in quantum compatible defects in SiC is on the rise due to their properties and the availability of both base material and mature processing [3].

The 4H polytype of SiC, 4H-SiC, hosts multiple candidate color centers. The silicon vacancy (V_{Si}) in 4H-SiC is a single-photon emitter (SPE) with favorable emission wavelengths in the near infrared (NIR) [4]. Room temperature coherent spin manipulation with several ms long coherence times reached under cryogenic conditions has also been shown [5]. The negatively charged V_{Si} at hexagonal (*h*) and pseudo-cubic (*k*) lattice sites emit light into three zero-phonon lines (ZPLs) [6]: V1 and V1' at 858 nm and 861 nm, respectively, assigned to different excited states of $V_{Si}^{-}(h)$, and V2 at 916 nm arising from $V_{Si}^{-}(k)$ [7]. In p-type material and upon thermal annealing the Si vacancy is transformed into the carbon antisite-vacancy pair ($C_{Si}V_C$ or CAV). The positive $C_{Si}V_C$ exhibits single-photon emission in the visible into multiple ZPLs at $640\,\text{nm}$ to $690\,\text{nm}$ [8]. Higher temperature annealing can convert the V_{Si} into complexes including the divacancy ($V_{Si}V_C$) and the nitrogen-vacancy or NV center ($V_{Si}N_C$). Both the neutral divacancy and negatively charged NV center in 4H-SiC exhibit single-photon emission characteristics in the infrared with emission wavelengths around 1050-1150 nm [9] and 1200-1300 nm [10], respectively.

A common feature of the known point defect SPEs in SiC is that only one of the charge states has been shown to be optically active, that is, single photon emission has been detected for only a specific range of Fermi levels. Hence, there is need for a strategy to control the defect charge state

in the material or device. Three possible routes have been discussed in the literature: (i) Fermi level design, (ii) optical control and (iii) electrical control. Fermi level design must be done prior to utilizing the defect, i.e., when performing the initial material choice. The impact of choosing epi-layers with different doping on the V_{Si}^{-} and $V_{Si}V_C^0$ emission intensities was shown in Ref. [11]. It is also possible to design regions of a device with different doping concentrations and embed defects selectively in each region, however, again, the choice must be made prior to operating the device. The second option is optical charge state control via dual laser excitation which was shown for the V_{Si}^{-} and $V_{Si}V_C^0$ in Ref. [12]. One laser initializes the charge state while the other drives the ground-to-excited-state transition. However, different excitations are likely needed for different defects, and without direct knowledge of the optical charge state transition levels in the bandgap, the initialization can be imprecise. Electrical control via biasing a device would enable a more controlled modulation of the defect charge state where the quantum emitter can be switched on and off at will. It should be noted that challenges also accompany the electrical approach, including the possibility of simultaneously charging or discharging close-lying defect states that may interfere with the measurement.

Electrical control over the defect charge state has been shown for the V_{Si} via biasing of a Schottky barrier diode (SBD) [13] or a p-i-n diode [14]. A p-i-n diode was also employed for electrical switching of the $V_{Si}V_C$ [15]. Furthermore, Ref. [13] provided an identification of the Si vacancy charge state transition levels in the band gap — enabling the design of precise control protocols for charge state manipulations within, e.g., an integrated SiC quantum communications device. Nonetheless, the mechanism behind the charge state switching experiments in SiC has been up for debate. Most works cite the band bending from the device and biasing as the primary driving force, while in certain cases, charge carrier capture and emission from nearby defects may also be involved.

In this work, we combine theoretical and experimental methods to study the mechanism for charge state switching of quantum emitters in 4H-SiC.

Methodology

Theoretical methods. Density functional theory (DFT) calculations were performed as implemented in the VASP code [16] and using the HSE06 hybrid functional [17] to estimate defect charge state transition levels for the V_{Si}, $V_{Si}V_C$ and the $C_{Si}V_C$. Formation energy diagrams were calculated according to the formalism outlined in Ref. [18] using finite-size corrections for charged defects [19]. Benchmarking of the methodology and comparison between theory and experiment for the V_{Si} is discussed in Ref. [13]. We employed 4H-SiC supercells containing 400 atoms, a 450 eV energy cut-off, the convergence criterion for the electronic self-consistent loop was set to 1×10^{-6} eV, and the forces were optimized to below 0.01 eV Å^{-1}. Both the lattice parameters and defect energetics were calculated using the HSE06 functional. The formation energy diagrams were calculated using Γ-only **k**-point sampling and are presented for Si-poor/C-rich conditions.

Device simulations in TCAD were performed using Sentaurus Device from Synopsys to investigate the electrical properties of Schottky barrier diodes containing defect traps. A simplified structure including the most important physical models for 4H-SiC was used to replicate the diode's response to various conditions such as the external bias. The simulations were performed for $T = 100$ K and $T = 300$ K, and for 0 V and -10 V applied bias.

Experimental methods. The mechanism for charge state control over point defects in 4H-SiC was studied experimentally using micro-structured n-type 4H-SiC samples. We employ $10\,\mu$m thick N-doped 4H-SiC epitaxial layers purchased from CREE, Inc. and having $\sim 1 \times 10^{15}$ cm^{-3} free carrier concentration as determined by capacitance-voltage (CV) measurements. Micro-sized near-cylindrical pillars of $3\,\mu$m radius were fabricated by photolithography and reactive ion etching using SiO_2 as a hard mask, see Figure 1(a). Point defects were introduced into the microstructures and surrounding material after fabrication by near-surface 21 keV He implantation to a fluence of 1×10^{11} cm^{-2}, resulting in an implanted defect profile peaking at ~ 150 nm below the surface according to SRIM simulations

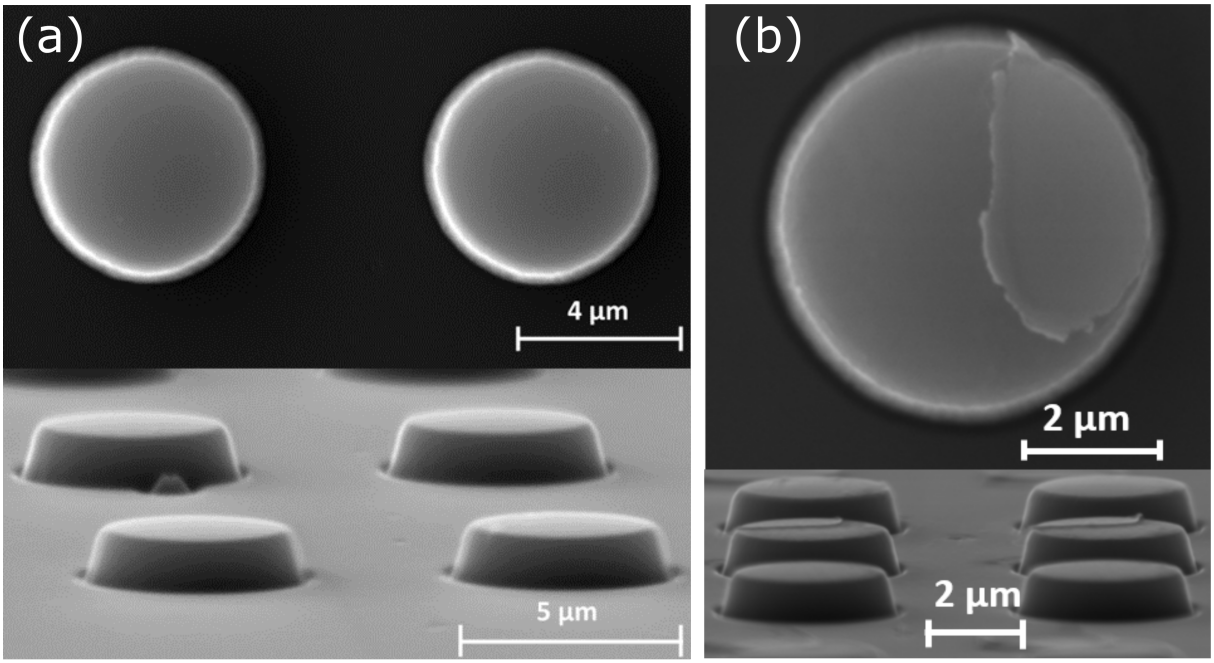

Fig. 1: Micropillar characterization. Scanning electron microscope (SEM) micrographs of micropillars with r=3 µm (a) seen from above (top panel) and in tilted side-view (bottom panel). (b) displays SEM micrographs of r=3 µm structures having Schottky contacts partly deposited on the top and side both from above (top) and at a tilted angle (bottom). The Ni metal layer is the thin film on the right side of the structure (top panel). An acceleration voltage of 20 kV was used.

[20]. The samples were post-annealed at 300 °C to alleviate some of the implantation damage such as interstitials. SBDs were formed on the micropillar and epi-layer surfaces to induce band bending, enabling charge state modification of the defects within the pillars. The SBDs were formed by depositing a thin layer (32 nm thickness) of Ni through a liftoff process with a photoresist mask. The mask only exposed parts of the micropillars, ensuring that the deposited Ni film only partly covered the structures, as shown in Figure 1(b). No additional heat treatments were performed after SBD formation. The pillars themselves were found to enhance the emission from the V_{Si} by a factor of ~ 1.5 as compared to the surrounding material, similar to that of a solid immersion lens.

The nanopillars were characterized using a JEOL JSM-IT300 scanning electron microscope (SEM) setup with a Everhardt-Thornley secondary electron detector and a LaB_6 filament, and the SEM images were acquired using a 10 or 20 kV acceleration voltage. Cathodoluminescence (CL) measurements were performed with a Delmic SPARC CL system integrated in the SEM chamber. Hyperspectral CL data was collected using an Andor Shamrock SR-193i spectrometer with a 300 l/mm grating and a charge-coupled device (CCD) Andor Newton DU940P-BU2 detector. We employed long pass filters with 500 nm or 700 nm cut-off wavelengths to block second order diffraction and record the near infrared (NIR) portion of the luminescence spectrum only. CL spectra were measured at 80 K using probe currents in the range 0.15-1 nA and 10 kV acceleration voltage, which translates to approximately $200-700$ nm penetration depth based on simulations in the software CASINO [21].

Results and Discussion

Formation energy diagrams calculated using hybrid density functional theory are shown in Figure 2 for the (a) V_{Si}, (b) $C_{Si}V_C$ and (c) $V_{Si}V_C$. The labels *h* and *k* refer to the lattice site type, i.e., hexagonal or pseudo-cubic. Note that the V_{Si} may exist in two different configurations while the $C_{Si}V_C$ and $V_{Si}V_C$ can inhabit four different configurations. Comparable findings have also been shown in, e.g., Refs. [22, 23, 24, 13]. The diagrams indicate the relative stability and cost of formation for the defect

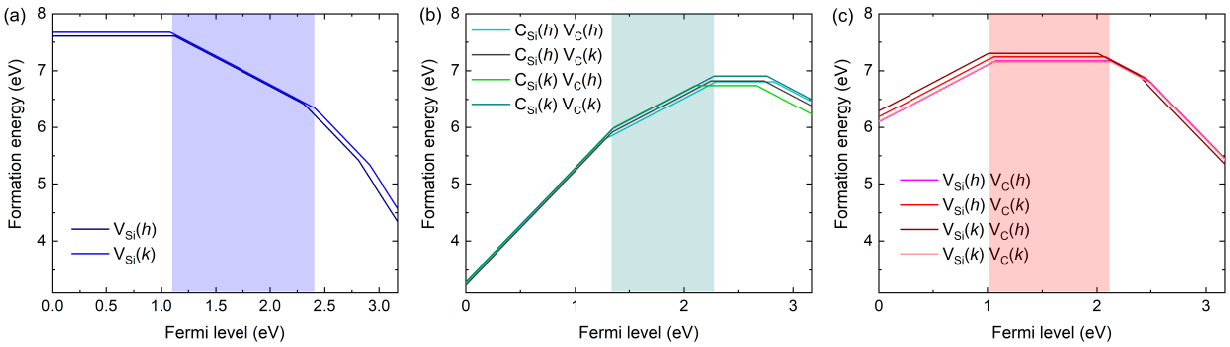

Fig. 2: Formation energy diagrams for the (a) Si vacancy, (b) carbon antisite-vacancy pair and (c) divacancy in 4H-SiC calculated using the HSE06 functional. 400-atom supercells are employed.

in different charge states as a function of the Fermi level. As indicated by the shaded areas, the emitting charge state (V_{Si}^-, $C_{Si}V_C^+$ and $V_{Si}V_C^0$) is preferred in a region near mid-gap only. In other words, in n-type material that is typically employed for SiC device fabrication, each of the emitters will occupy a dark charge state, and additional energy must be added to facilitate the single-photon emission.

Controlling the charge states of point defects relies on secure identification of the defect charge transition levels in the band gap. For the Si vacancy, the (2-/3-) and (-/2-) transition levels were assigned to the S1 and S2 peaks in deep level transient spectroscopy (DLTS) spectra of irradiated 4H-SiC at 0.4 eV and 0.7 eV below the conduction band edge (E_C), respectively [13]. A recent work employed a similar methodology for the $C_{Si}V_C$ and tentatively assigned the EH_4 and EH_5 DLTS peaks to the (+/0) transition of the $C_{Si}V_C$ at $E_C - 1.0$ eV to 1.1 eV [25]. Another work also experimentally assigned the (+/0) charge transition level of the $C_{Si}V_C$ to $E_C - 1.1$ eV using photo-electron paramagnetic resonance (photo-EPR) [26]. In the case of the divacancy, however, experimental identification of the transition levels is missing. There are multiple reasons for this. On the one hand, divacancy formation occurs via diffusion and complex formation when samples containing Si vacancies are annealed at $800\,^\circ$C to $1000\,^\circ$C. Hence, from the perspective of DLTS measurements, high defect concentrations are often necessary, above the limit of $\sim 0.2 N_D$. Furthermore, Fig. 2(c) demonstrates that the (0/-) transition level, which has to be crossed by the Fermi level in order to induce charging/discharging of $V_{Si}V_C^0$ in n-type 4H-SiC, is found deep in the band gap. This implies that electron emission only takes place at high temperatures, and detection of the relevant levels may suffer from, e.g., broadening of the DLTS peaks and increased leakage for Schottky diodes causing noisy spectra.

In Ref. [13], the emission intensity from the V_{Si}^- was manipulated by biasing a Schottky barrier diode (SBD). The effect was attributed to the band bending caused by the built-in and induced electric fields of the SBD. Figure 3 shows TCAD simulations demonstrating the band bending incurred by the SBD at 100 K and 0 V (top), and 300 K and -1 V (bottom). The shaded colored areas illustrate the distances from the Schottky contact/4H-SiC interface where the bright charge state of the V_{Si} (blue), $C_{Si}V_C$ (green) and $V_{Si}V_C$ (red) is promoted by the band bending as they fall above the Fermi level. For the 100 K and 0 V case, the V_{Si}^- is preferred in a larger volume of the space charge region than $C_{Si}V_C^+$ and $V_{Si}V_C^0$. The difference between the three defects is smaller for the 300 K and -1 V case. In other words, biasing the SBD (or another device geometry) at different temperatures is a highly suitable strategy for controlling the charge state of the single-photon emitter. The key point will then be to integrate the defect at a controlled location where it can be manipulated by moderate electric fields. Interestingly, the electric fields employed herein and in Ref. [13], while far below those traditionally employed for power devices, are in the range of those used in integrated circuits (ICs).

The cathodoluminescence (CL) spectrum in Figure 4(a) was collected at 80 K and demonstrates the V_{Si}-related emission arising in the near-infrared (NIR) portion of the spectrum. The negatively charged Si vacancy is associated with three zero-phonon lines: V1, V1' and V2. V1 and V1' are overlapping but still clearly observed in Fig. 4(a), while V2 overlaps with the phonon side-band (PSB) of the V_{Si}.

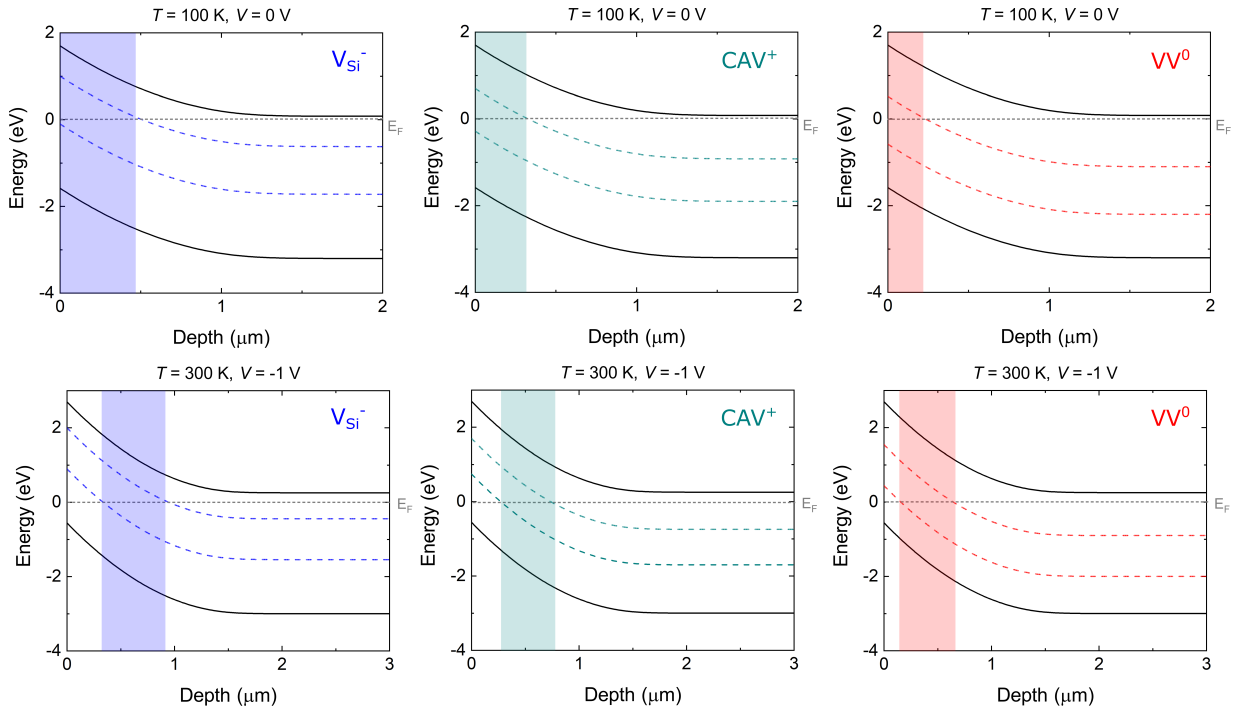

Fig. 3: Band bending caused by electric fields simulated using the Sentaurus Device simulator with deposited SBD. Top panels: without applied bias and at 100 K. Bottom panels: with −1 V applied bias and at 300 K. The spatial regions where the bright charge state is dominant are shown by colored areas in blue for V_{Si}^{-}, green for $C_{Si}V_C^{+}$ and red for $V_{Si}V_C^{0}$. Parts of the data were also shown in Ref. [13].

The V_{Si}-related emission is found to be stronger when it originates from the r=3 µm microstructures as compared to the neighboring epi-layer regions (not shown) by a factor of ~ 1.5.

To induce near-surface band bending and obtain defect charge-state control, Schottky barrier diodes were fabricated on portions of the micropillar surfaces, as shown in Fig. 1(b). Figures 4(b) and 4(c) compare V_{Si}-related emission (filtered in a 8 nm interval centered at 858 nm) from a r=3 µm pillar acquired at different locations surrounding the SBD (metal edge marked by the green dashed line). The depletion region is estimated to protrude ∼2.3 µm from the Schottky diode by using the depletion approximation (marked by the blue dashed line). Note that the estimate was made for a downward extension of the space charge region into the sample while we are monitoring both the lateral distribution and extension from the pillar sidewall, which adds to the uncertainty of the estimate. Intriguingly, the emission from the V_{Si} is stronger from within the depletion region as compared to further away, with the emission decreasing continuously towards the edge of the micropillar. Hence, the CL intensity maps in Fig. 4(b)-(c) demonstrate that the emission intensity is enhanced within the depletion region of the SBD, and lend support to the theory represented by the TCAD simulations in Fig. 3. Finally, the positively charged $C_{Si}V_C$ is considered. The $C_{Si}V_C$ emits single photons at room temperature, and at low temperatures the emission can be seen as a set of sharp lines named the AB-lines and having emission peaks at A1= 648.7 nm, A2= 651.8 nm, A3= 665.1 nm, A4= 668.5 nm, B1= 671.7 nm, B2= 673.0 nm, B3= 675.2 nm and B4= 676.5 nm [8]. The $C_{Si}V_C$ was heterogeneously distributed across the micropillar surface and only present in certain locations, often with several µm separating each detectable defect or more likely defect cluster. The Si vacancy, on the other hand, was found across the whole sample surface but with some fluctuations in emission intensity indicating heterogeneity in the spatial distribution of this defect. From the resulting dataset, the spectrum with the most intense emission from $C_{Si}V_C$ was selected as the signal, and a spectrum from a neighboring area showing no $C_{Si}V_C$ emission was used as the background (both of these spectra were acquired from the same micropillar). The background was then subtracted from the signal. CL spectra showing the $C_{Si}V_C$ emission, background and background-subtracted $C_{Si}V_C$ signal are shown in Figure 5(a).

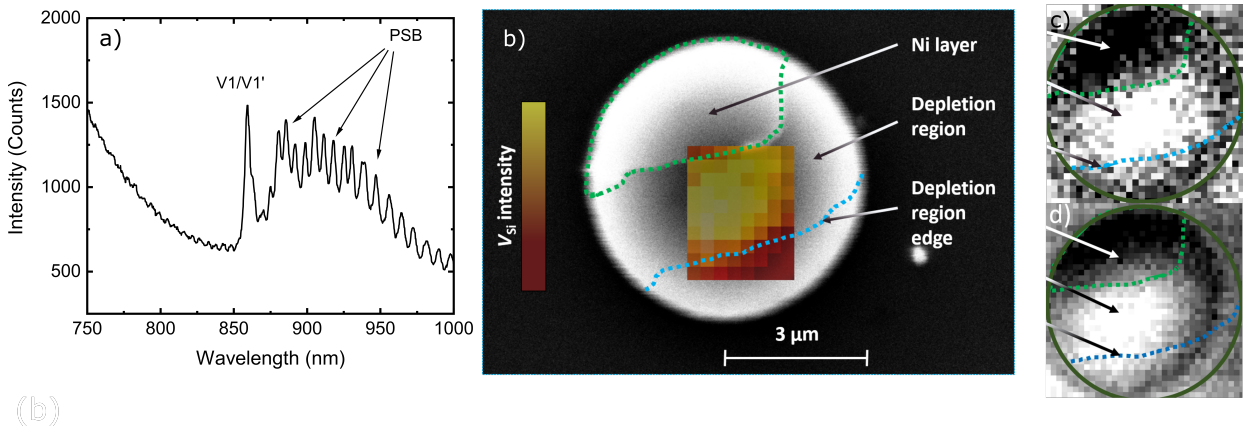

Fig. 4: (a) CL spectrum of He-implanted (21 keV) 4H-SiC showcasing the near infrared (NIR) emis-sion after applying a 700 nm long-pass filter. Panels (b)-(d) show CL false color maps of V_{Si} emission surrounding an SBD on a r=3 µm micropillar. The Ni layer and depletion region edge, extending to ∼2.3 µm from the metal contact, are bordered by green and blue dotted lines, respectively. An accel-eration voltage of 20 kV and probe current of 0.3 nA were used for the electron beam at 80 K. The V_{Si}-related emission is filtered using a bandwidth of 8 nm centered at 858 nm.

The ZPLs labeled the AB-lines assigned to the $C_{Si}V_C$ appear in an overlapping region. Figure 5(b) contains the high-resolution background-subtracted CL spectrum from the $C_{Si}V_C$ and tentatively assigns the different spectral features to their specific origins, after the assignments made in Ref. [8]. The most dominant feature appears to be B2 with the remaining lines being significantly weaker, in contrast to Ref. [8] where B3 was the dominant feature. However, this was for p-type material, which may in part explain the intensity differences for emission from the various $C_{Si}V_C$ configurations (*hh*, *hk*, *kh* and *kk*). To study the $C_{Si}V_C$ emission lineshape in more detail we roughly group the background subtracted $C_{Si}V_C$ signal into the (mainly) B2 zero-phonon line (pink shaded area) and the phonon side band (blue shaded area), see Fig. 5(a). The signal intensities in the zero-phonon line and the phonon side band, respectively, were integrated and the resulting areas used to estimate the Debye-Waller (DW) factor for the $C_{Si}V_C^+$, yielding a value of 13 %. Note that the phonon side band may encompass

ZPLs from other $C_{Si}V_C$ configurations or defect species, adding to the uncertainty for the estimate of DW factor. By considering the sharp feature at 1.7 eV as a ZPL, and removing it from the integrated area, we instead arrive at a DW factor of 14 %, constituting a change of ∼ 8 %. Moreover, as shown by Fig. 5(b), all $C_{Si}V_C$ configurations appear to contribute to the lineshape. However, as B2 is substantially stronger than the other features, this error is small. As an exact characterization of the full lineshape presented in Fig. 5(a) is not available at this time, we estimate the DW factor for emission from the $C_{Si}V_C^+$ at 13.5 ± 0.5 %. The DW factor is an important aspect in assessing the suitability of a color center for a specific quantum application as both bright emission and identical photons are typically important parameters. The heterogeneous distribution of $C_{Si}V_C$ made a verification of any emission enhancement or reduction effect caused by the Schottky diodes challenging. We were unable to locate $C_{Si}V_C$ defects in more than one or two areas (300 × 300 nm) on each micropillar. However, although the $C_{Si}V_C$ was clearly detectable and exhibiting a strong signal in certain locations in the sample with metal deposited on the surface, no such signal could be found for a similar sample without such metal deposition — despite the same implantation conditions being used. This may indicate that the emission intensity from the $C_{Si}V_C^+$ is enhanced due to band bending from the Schottky diode causing preferential population of the positive charge state, but can alternatively be explained by random clustering of $C_{Si}V_C$ defects in specific locations. Regardless, further studies of samples with higher $C_{Si}V_C$ defect concentrations are needed to resolve the open questions.

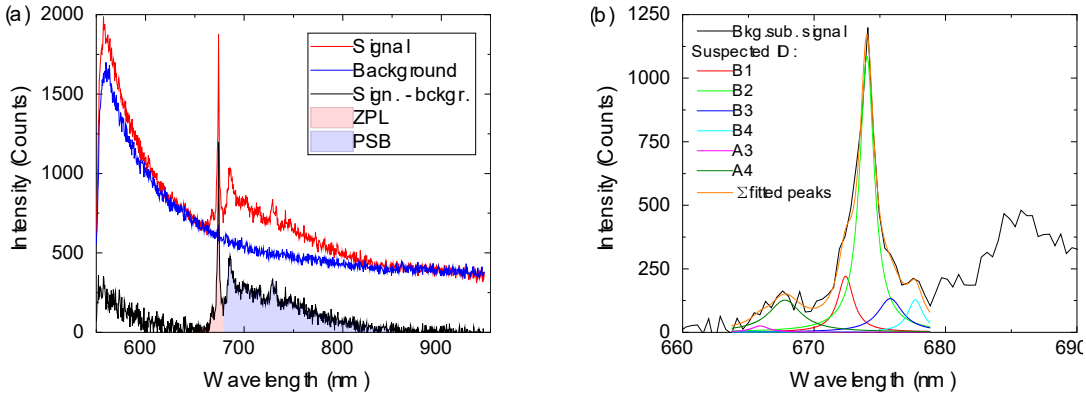

Fig. 5: Emission from the $C_{Si}V_C^+$. (a) CL measurement from within a micropillar showing emission from the $C_{Si}V_C$ in red, emission from a neighboring area still on the structure but without visible $C_{Si}V_C$ emission in blue, and background-subtracted $C_{Si}V_C$ emission in black. Colored areas indicate the $C_{Si}V_C$-related zero-phonon line (ZPL) in pink and the phonon side band (PSB) in blue. (b) High resolution CL spectrum (after background subtraction) focusing on the $C_{Si}V_C$ ZPL and deconvoluting the contributions from different configurations (separated into the ZPLs B1-B4 and A3-A4). The CL spectra were measured using a 0.1 nA probe current and an acceleration voltage of 5 kV at 80 K, using a spectrometer entrance slit of 1.25 mm and a 500 nm long-pass filter. The exposure area was approximately 330×330 nm^2.

Concluding Remarks

We study the impact of charge state identification and control on the manipulation of emission intensities from quantum emitters in 4H-SiC. Density functional theory calculations to construct formation energy diagrams are a useful tool for estimating charge transition levels, as discussed for the Si vacancy (V_{Si}), carbon antisite-vacancy pair ($C_{Si}V_C$) and divacancy ($V_{Si}V_C$) herein. Based on the extracted charge state transition levels, TCAD simulations indicate how a color center can be positioned and controlled within, e.g., a quantum communications device. For a Schottky diode formed on low doped n-type 4H-SiC ($\sim 1 \times 10^{15}$ cm^{-3}), mild biasing within the -2 V to 2 V range is sufficient to establish defect charge-state control over $\sim$1 µm depth.

To confirm the hypothesis that band bending induced by the SBDs promotes selective charge-state occupation of the bright state, micropillars were formed by photolithography and etching of 4H-SiC epi-layers. Ni Schottky contacts were deposited on parts of the surface and sides of the pillars to form the depletion region. Cathodoluminescence (CL) false color maps demonstrate that the V_{Si}^- emission intensity peaks within the depletion region center and drops towards the edge. For the $C_{Si}V_C$ case, the heterogeneous distribution and low defect density prevent a secure monitoring of the field dependence of the emission, however, our results indicate that the AB-lines are enhanced in the electric field of the SBD. The divacancy was not present in the samples studied herein but similar behavior is expected. In short, the mechanism behind previously shown intensity modulation is confirmed, which may contribute to electrically controllable quantum devices based on intrinsic defects in SiC.

Acknowledgements

The work of MEB was supported by an ETH Zürich Postdoctoral Fellowship. Financial support was kindly provided by the Research Council of Norway and the University of Oslo through the frontier research projects FUNDAMeNT (no. 251131, FriPro ToppForsk-program) and QuTe (no. 325573). The Research Council of Norway is acknowledged for the support to the Norwegian Micro- and Nano-Fabrication Facility, NorFab, project number 295864. The computations were performed on resources

provided by UNINETT Sigma2 — the National Infrastructure for High Performance Computing and Data Storage in Norway.

References

[1] J. R. Weber, *et al.*, PNAS 107, 8513 (2010).

[2] M. W. Doherty, *et al.*, Phys. Rep. 528, 1 (2013).

[3] N. T. Son, *et al.*, Appl. Phys. Lett. 116, 190501 (2020).

[4] M. Widmann, *et al.*, Nat. Mater. 14, 164 (2015).

[5] D. Simin, *et al.*, Phys. Rev. B 95, 161201(R) (2017).

[6] E. Janzén, *et al.*, Physica B 404, 4354 (2009).

[7] V. Ivády, *et al.*, Phys. Rev. B 96, 161114(R) (2017).

[8] S. Castelletto, *et al.*, Nat. Mater. 13, 151 (2014).

[9] D. J. Christle, *et al.*, Nat. Mater. 14, 160 (2015).

[10] H. J. von Bardeleben, *et al.*, Phys. Rev. B 94, 121202(R) (2016).

[11] N. T. Son and I. G. Ivanov, Journ. Appl. Phys. 129, 215702 (2021).

[12] G. Wolfowicz, *et al.*, Nat. Comm. 8, 1876 (2017).

[13] M. E. Bathen, *et al.*, npj Quantum Information 5, 111 (2019).

[14] M. Widmann, *et al.*, Nano Lett. 19, 7173 (2019).

[15] C. P. Anderson, *et al.*, Science 366, 1225 (2019).

[16] G. Kresse and J. Furthmüller, Phys. Rev. B 50, 17953 (1996).

[17] J. Heyd, G. E. Scuseria and M. Ernzerhof, Journ. Chem. Phys. 118, 8207-8215 (2003).

[18] C. Freysoldt, *et al.*, Rev. Mod. Phys. 86, 253 (2014).

[19] C. Freysoldt, J. Neugebauer and C. G. van de Walle, Phys. Rev. Lett. 102, 253 016402 (2009).

[20] J. F. Ziegler, M. D. Ziegler and J. P. Biersack, Nuclear Inst. and Methods in Physics Research B 268, 1818-1823 (2010).

[21] D. Drouin, *et al.*, Scanning 29, 92-101 (2007).

[22] T. Hornos, A. Gali and B. G. Svensson, Mater. Sci. Forum 679-680, 261–264 (2011).

[23] K. Szasz, *et al.*, Phys. Rev. B 91, 121201(R) (2015).

[24] A. Beste *et al.*, Phys. Rev. B 98, 214107 (2018).

[25] R. Karsthof, M. E. Bathen, *et al.*, Phys. Rev. B 102, 184111 (2020).

[26] N. T. Son, *et al.*, Appl. Phys. Lett. 11, 212105 (2019).